This is an open access article published under an ACS AuthorChoice License, which permits copying and redistribution of the article or any adaptations for non-commercial purposes.

THE JOURNAL OF PHYSICAL CHEMISTRY C

Article

pubs.acs.org/JPCC

Reactivity of Perovskites with Water: Role of Hydroxylation in Wetting and Implications for Oxygen Electrocatalysis

Kelsey A. Stoerzinger,[†] Wesley T. Hong,[†] Gisele Azimi,[‡,▽] Livia Giordano,[‡,§] Yueh-Lin Lee,[‡] Ethan J. Crumlin,[∥] Michael D. Biegalski,[⊥,○] Hendrik Bluhm,[#] Kripa K. Varanasi,*[,‡] and Yang Shao-Horn*[,†,‡]

[†]Department of Materials Science and Engineering and [‡]Department of Mechanical Engineering, Massachusetts Institute of Technology, Cambridge, Massachusetts 02139, United States

[§]Dipartimento di Scienza dei Materiali, Università di Milano-Biocca, Milano 20125, Italy

[∥]Advanced Light Source, Lawrence Berkeley National Laboratory, Berkeley, California 94720, United States

[⊥]Center for Nanophase Material Sciences, Oak Ridge National Laboratory, Oak Ridge, Tennessee 37831, United States

[#]Chemical Sciences Division, Lawrence Berkeley National Laboratory, Berkeley, California 94720, United States

Supporting Information

ABSTRACT: Oxides are instrumental to applications such as catalysis, sensing, and wetting, where the reactivity with water can greatly influence their functionalities. We find that the coverage of hydroxyls (*OH) measured at fixed relative humidity trends with the electron-donor (basic) character of wetted perovskite oxide surfaces. Using ambient pressure X-ray photoelectron spectroscopy, we report that the affinity toward hydroxylation, coincident with strong adsorption energies calculated for dissociated water and hydroxyl groups, leads to strong H bonding that is favorable for wetting while detrimental to catalysis of the oxygen reduction reaction (ORR). Our findings provide novel insights into the coupling between wetting and catalytic activity and suggest that catalyst hydrophobicity should be considered in aqueous oxygen electrocatalysis.

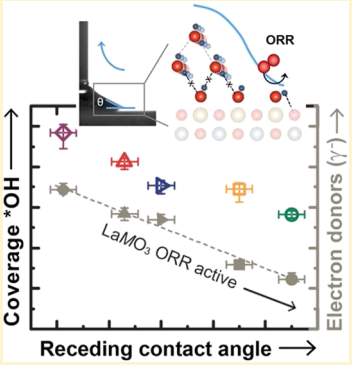

INTRODUCTION

The interaction of oxides with water plays a critical role in a large number of applications,[1−5] including water purification, gas sensing and separation, photoelectrochemistry, electrocatalysis, and wetting. The solid/liquid interface between water and oxides is one of the fundamental components in electrochemistry and electrocatalysis. The hydroxylation and binding of surface adsorbates[6,7] on oxides can greatly influence the adsorptive and wetting properties[4,5,8,9] and catalytic activity.[10−14] These observations have been rationalized by the change in polarity induced by surface hydroxyl species.[8,13] Here we evaluate intrinsic properties of oxide surfaces that can bridge wetting and activity for oxygen electrocatalysis.

Directly measuring hydroxylation and surface adsorbates in liquid water and correlating these species to wetting and catalytic activity is challenging—particularly for oxide systems where both the adsorbate and catalyst contain oxygen. Conventional contact angle measurements do not provide information at the molecular level on water adsorption energetics, the degree of hydroxylation, or interfacial hydration structure.[15] On the other hand, the molecular interaction of water with complex, catalytically active metal oxide surfaces has been studied using traditional surface science microscopy and spectroscopy techniques but only in ultrahigh vacuum and often at cryogenic temperatures.[16−18] Here we take advantage of recent advances in ambient pressure X-ray photoelectron spectroscopy (AP-XPS)[19−21] to measure the extent of surface hydroxylation and adsorption of water on oxide surfaces.

In this report, we utilize the flexibility of the perovskite surface chemistry ($LaMO_3$, M = Cr to Ni) to show that increasing hydroxylation measured from AP-XPS scales with increasing hydrophilicity from contact angle measurements. Both hydroxylation and surface electron-donating character exhibit a W shape as a function of d electrons, which is in agreement with computed energetics of hydroxylation on MO_2- and LaO-terminated surfaces from density functional theory (DFT). Moreover, decreasing surface hydrophilicity correlates with increasing catalytic oxygen reduction reaction (ORR) activities in basic solution.

EXPERIMENTAL AND THEORETICAL METHODS

Thin Film Growth and Characterization. Films were fabricated by pulsed laser deposition (PLD) on single crystal (001)-oriented 0.5 wt % Nb-doped $SrTiO_3$ substrates with a dimension of 10 × 5 × 0.5 mm (Crystec, GmbH). The PLD

Received: July 10, 2015
Published: July 15, 2015

Downloaded via 151.64.0.206 on November 25, 2020 at 15:08:47 (UTC).
See https://pubs.acs.org/sharingguidelines for options on how to legitimately share published articles.

© 2015 American Chemical Society

DOI: 10.1021/acs.jpcc.5b06621
J. Phys. Chem. C 2015, 119, 18504−18512

targets of $LaMnO_3$ and $LaFeO_3$ were purchased (Praxair, Inc.) for thin film deposition. The $LaCoO_3$ PLD target was synthesized using a solid-state reaction from stoichiometric mixtures of La_2O_3 and Co_3O_4 (Alfa Aesar, USA) and sintered at 1450 °C to 90% theoretical density. $LaCrO_3$ and $LaNiO_3$ PLD targets were synthesized by the glycine−nitrate combustion reaction. Stoichiometric quantities of nitrate precursors—$La(NO_3)_3{\cdot}6H_2O$ (99.999% metal basis, Alfa Aesar), $Ni(NO_3)_3{\cdot}6H_2O$ (99.999% metal basis, Sigma-Aldrich), or $Cr(NO_3)_3{\cdot}9H_2O$ (99.99% metal basis, Sigma-Aldrich)—were dissolved in Milli-Q water (18 MΩ cm), to which glycine was added. The mixture was heated and allowed to slowly evaporate and then heated at 400 °C under an air atmosphere for 4 h. The resulting powder was ground, pressed, and sintered at 800 °C under an air atmosphere for 12 h. The resulting pellet was then reground, pressed, and sintered a second time at the same conditions.

PLD was performed using a KrF excimer laser (λ = 248 nm) at a pulse frequency of 10 Hz and laser fluence of ~1.50 J cm^{-2}. The ~20 nm films of $LaCrO_3$, $LaMnO_3$, $LaFeO_3$, $LaCoO_3$, and $LaNiO_3$ were deposited under the conditions shown in Table S1. Thin film X-ray diffraction (XRD) was performed using a four-circle diffractometer (Bruker D8, Germany) in normal and off-normal configurations (Figure 1a,b) with relaxed lattice

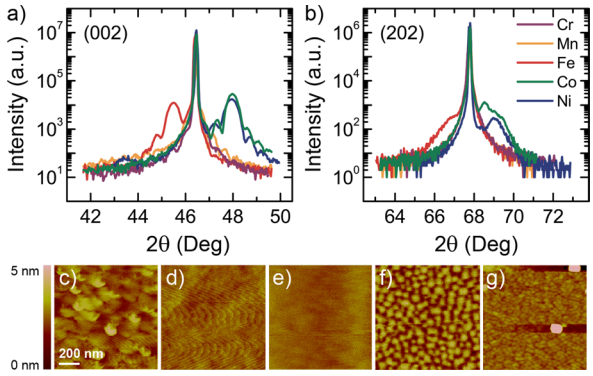

Figure 1. Characterization of $LaMO_3$ films, where M = Cr (purple), Mn (orange), Fe (red), Co (green),[23] and Ni (blue). High-resolution X-ray diffraction (XRD) in the (a) normal configuration (002), with thickness fringes indicating high film quality, and (b) off-normal configuration (202). Atomic force microscopy (AFM) of film surfaces and RMS roughness: (c) $LaCrO_3$ 0.4 nm, (d) $LaMnO_3$ 0.2 nm, (e) $LaFeO_3$ 0.2 nm, (f) $LaCoO_3$ 0.5 nm,[23] (g) $LaNiO_3$ 1.6 nm. The 200 nm scale bar is the same for all images, and the color scale is 0−5 nm.

parameters and associated strain in Table S2. The film thickness was estimated using the thickness fringes in the high-resolution $\theta-2\theta$ scans of the (002) diffraction peaks ("Epitaxy" software, Panalytical). Film surface morphologies were examined by atomic force microscopy (AFM, see Figure 1c−g and Table S3) (Veeco), with root-mean-square (RMS) roughness values ≤0.5 nm, except for $LaNiO_3$ (1.6 nm). Some particles were observed on the $LaNiO_3$ surface, the coverage of which was estimated from 100× optical microscopy images to be <3.3%. These particles are expected to be stoichiometric $LaNiO_3$ fragmented from the target during deposition,[22] and the difference in surface area compared to a flat one is <1.9%.

Ambient Pressure X-ray Photoelectron Spectroscopy (AP-XPS). AP-XPS was collected at Beamline 11.0.2[23,24] at Lawrence Berkeley National Laboratory's (LBNL) Advanced Light Source (ALS). Films were placed onto a ceramic heater,[25] with a thermocouple mounted directly onto the sample surface for temperature measurements, and isolated from the sample holder clips with an Al_2O_3 spacer. A piece of Au foil, scraped clean with a razor, was placed on top of a corner of the sample for calibration of the incident photon energy, referenced to the Au 4f at 84.0 eV. The binding energy (BE) of the oxide O 1s bulk peak was calibrated by defining the C 1s of adventitious carbon present on the sample prior to cleaning at 284.8 eV. All subsequent spectra are aligned relative to this O 1s peak.

Care was taken to reduce the beam flux so issues such as coking were not observed. This was achieved by limiting the dispersive and nondispersive slits to 15 and 50 μm, respectively, and the X-ray beam shutter was kept closed between scans. The change in coverage of *OH for a given change of relative humidity (RH) was slightly less comparing among fresh regions of the sample versus comparing the change in coverage of *OH at the same location. However, coverage of *OH in both cases showed the same saturation behavior with RH,[23] and we report coverage of *OH only at the most humid condition. We attribute the differences from beam irradiation to an increase in the dissociation constant of H_2O,[26] effectively reducing the barrier for hydroxylation. Because the irradiation was constant among materials and coverage of *OH shows a saturation-like behavior with RH, we do not expect adverse effects in comparison among materials.

The samples were cleaned by heating to 300 °C in $p(O_2)$ of 100 mTorr (measured by a calibrated capacitance gauge) until clean of carbon (Figure S1). A small amount of SO_x species was observed in the O_2 environment from displacement of residue species from the chamber walls (for an estimation of the contribution to the O 1s spectra, see our previous publication[23]), which reduced to a negligible quantity upon introduction of H_2O. After characterization of the clean surface in O_2, the chamber was evacuated to a pressure $<1.5 \times 10^{-7}$ Torr, and $p(H_2O)$ of 100 mTorr was introduced into the chamber. The H_2O was prepared from deionized water (Millipore, >18.2 MΩ cm) and degassed by several freeze−pump−thaw cycles. Contaminants in gaseous species have been previously noted to affect wetting,[27] and any possible influence from their presence has been carefully assessed. The sample was then cooled in increments of 25 °C down to a final temperature of 25 °C, keeping the chamber pressure constant at $p(H_2O)$ of 100 mTorr. At every temperature, the O 1s and C 1s core level spectra were collected, and at 100 °C increments as well as 25 °C, the La 4d and transition metal 3p core level spectra were also collected. All spectra were taken at an incident energy of 735 eV. The C/O relative sensitivity factor (RSF) was experimentally obtained by measuring the respective 1s core levels of 250 mTorr CO_2 gas. This provided a value of 0.86 ± 0.03:1 (O 1s:C 1s) for an incident photon energy of 735 eV. This value depends on the experimental geometry and potentially the chamber pressure and should be measured for each experimental run.

Coverages of surface oxygenated species (Tables S4 and S5) were estimated from the O 1s spectra using a multilayer electron attenuation model,[28,29] as discussed in ref 23. This model takes as an input the oxygen atomic density, N, the inelastic mean free path (IMFP, λ), and the photoelectron emission angle. While the coverages of *OH and *H_2O discussed in the text give a more physical comparison among materials, the relative differences among $LaMO_3$ materials can also be seen in the percent contribution of these species to the total O 1s counts in Table S6. A small amount of adventitious

DOI: 10.1021/acs.jpcc.5b06621
J. Phys. Chem. C 2015, 119, 18504−18512

carbon was also observed at lower temperatures (Table S6) and is assumed to sit atop the surface uniformly and not influence the results.

Contact Angle Measurements. Contact angles for the three probe liquids of diiodomethane (DIM, Alfa Aesar), ethylene glycol (EG, Alfa Aesar), and deionized water (18 MΩ cm, Millipore) were measured using a Ramé-Hart M500-advanced goniometer. The advancing and receding contact angles were measured by adding/removing water from a 5 μL droplet on the surface at the rate of 0.2 μL/s. This ensures that the capillary number is always low enough for accurate measurements. A smaller droplet volume was used with other probe liquids due to the lower contact angle and small sample size. Measurements on a second $LaMnO_3$ film yielded a water advancing angle within 2° and a receding angle within 5° of that measured on the first film. Repeat measurements on the first film after drying yielded values within the same range.

Electrochemical Measurements. Electrical contacts were applied to the back of the conductive Nb-doped $SrTiO_3$ substrate, as reported previously.[30] Gallium−indium eutectic (Sigma-Aldrich, 99.99%) was scratched into the Nb-doped $SrTiO_3$, and a Ti wire (Sigma-Aldrich, 99.99%) was affixed with silver paint (Ted Pella, Leitsilber 200). The back and sides of the electrode, as well as the wire, were covered with a nonconductive, chemically resistant epoxy (Omegabond 101), so only the catalyst surface was exposed to the electrolyte.

Electrochemical measurements were conducted with a Biologic SP-300 potentiostat in an ∼120 mL solution of 0.1 M KOH, prepared from deionized water (Millipore, >18.2 MΩ cm) and KOH pellets (Sigma-Aldrich, 99.99%). Potentials were referenced to a saturated Ag/AgCl electrode (Pine), calibrated to the reversible hydrogen electrode (RHE) scale in 0.1 M KOH. Oxygen reduction reaction (ORR) measurements were carried out in an electrolyte presaturated by bubbling O_2 for at least 45 min and under continuous O_2 bubbling (Airgas, ultrahigh-grade purity). ORR cyclic voltammetry (CV) at a scan rate of 10 mV s^{-1} is plotted corrected for capacitance by averaging the forward and backward sweeps. Electrical impedance spectroscopy (EIS) was performed at the open circuit voltage with an amplitude of 10 mV. Potentials were corrected for the electrolyte/cell resistance from the high-frequency intercept of the real impedance (45 Ω).

Density Functional Theory Calculations. Density functional theory calculations with Hubbard U correction (DFT +U)[31,32] were carried out with a periodic approach and plane wave basis set, as implemented in the VASP code.[33,34] Core electrons were described with the Projector Augmented Wave (PAW) method,[35] and the plane wave cutoff was set to 450 eV. We used the gradient-corrected Perdew−Wang 91 (PW91) functional[36] and the optimal effective *U* values on the transition metal d electrons determined by fitting the formation enthalpies of oxides.[37,38]

Full optimizations of bulk perovskite structures for each $LaMO_3$ (*M* = Cr, Mn, Fe, Co, Ni) were performed using the experimental symmetry at low temperature[39−42] based on the ferromagnetic ordering in order to use a consistent and tractable set of magnetic structures, except for $LaFeO_3$, where we considered a G-type antiferromagnetic ordering to account for the higher Néel temperature.[39,43] Internally relaxed pseudocubic 2 × 2 × 2 perovskite supercells were then constructed with effective perovskite lattice constants obtained by taking the cube root of the normalized volume (per formula unit) of the fully relaxed perovskites. The fully relaxed perovskite bulk coordinates were used as initial atomic positions, and for these calculations the reciprocal space unit cell was sampled by a (2 × 2 × 2) *k*-point mesh. The (001) orientation of $LaMO_3$ pseudocubic perovskite is polar, and symmetric seven-layer slab models were employed in order to cancel the related dipole moment perpendicular to the surface. The (2 × 2) (001) LaO- and MO_2-terminated slab models have been constructed using the 2 × 2 × 4 pseudocubic perovskite supercells with 10 Å vacuum space inserted between the two terminations of a (001) slab and removal of an MO_2 layer for the seven-layer (001) LaO slab (and removal of a LaO layer for the seven-layer (001) MO_2 slab). Internal relaxations of the (001) slab coordinates were performed without adsorbates. Previous work has shown that this approach gives a satisfactory description of the surface properties of these systems.[38,44] The adsorbates (dissociatively adsorbed H_2O, *OH, and *H) were then adsorbed on one side of the slab, and the adsorbate coverage varied from 1/4 to 1 monolayer (ML), where 1 ML corresponds to one adsorbate per surface metal atom. The bottom two layers of the slab models were kept fixed, while the adsorbate and remaining slab coordinates were internally relaxed. A (2 × 2 × 1) *k*-point sampling was used for such slab models.

Stability of the (dissociatively adsorbed) H_2O, *H, and *OH at the experimental condition was estimated using the chemical potentials of H_2O, H_2, and O_2 as detailed in the Supporting Information. By setting the chemical potential of oxygen to be at the condition of T = 25 °C and 1.5 × 10^{-7} Torr partial pressure of oxygen (the lowest detectable limit in the AP-XPS chamber) and the $p(H_2O)$ to be 0.1 Torr, we estimate the corresponding effective applied potential at the experimental condition to be 1.20 V relative to the standard hydrogen electrode (SHE, a_{H^+} = 1). This is comparable to the equilibrium potential of O_2/H_2O in O_2-saturated liquid water for ORR measurements, 1.23 V relative to the reversible hydrogen electrode. The adsorption free energies, G_{ad}, were then computed with respect to the H_2O, H_2, and O_2 chemical potential references at the effective applied potential of 1.2 V vs SHE as detailed in the Supporting Information.

RESULTS AND DISCUSSION

Determining Coverage of *OH at Fixed Relative Humidity. We examined the reactivity of water vapor on (001)-oriented $LaMO_3$ film surfaces using AP-XPS by performing water isobar experiments to deconvolute the spectra. Quantifying by a multilayer electron attenuation model (Figure 2a), we compare the component species at fixed relative humidity (RH, Figure 2b). The surfaces were cleaned *in situ* by heating in O_2 (Figure S1) before exposure to water vapor. Water isobar measurements (p_{H_2O} = 100 mTorr) were performed by cooling, reaching a final RH of ∼0.3% at 25 °C. The O 1s and C 1s spectra of all $LaMO_3$ showed similar features (Figures S2−S5 and ref 23), and the intensities varied with RH. Pronounced changes in the isobar O 1s spectra are noted with increasing RH. This evolution has been discussed in great detail for the case of $LaCoO_3$ in ref 23, and we here only summarize the main trends.

After a surface was cleaned in O_2 at 300 °C, it remained free of carbon as shown by the C 1s region. The lowest binding energy (BE) is characteristic of oxygen in bulk coordination, while that at ∼2.8 eV higher BE was shown by depth profiling (Figures S3 and S4, ref 23) to be located at the surface. At

DOI: 10.1021/acs.jpcc.5b06621
J. Phys. Chem. C 2015, 119, 18504−18512

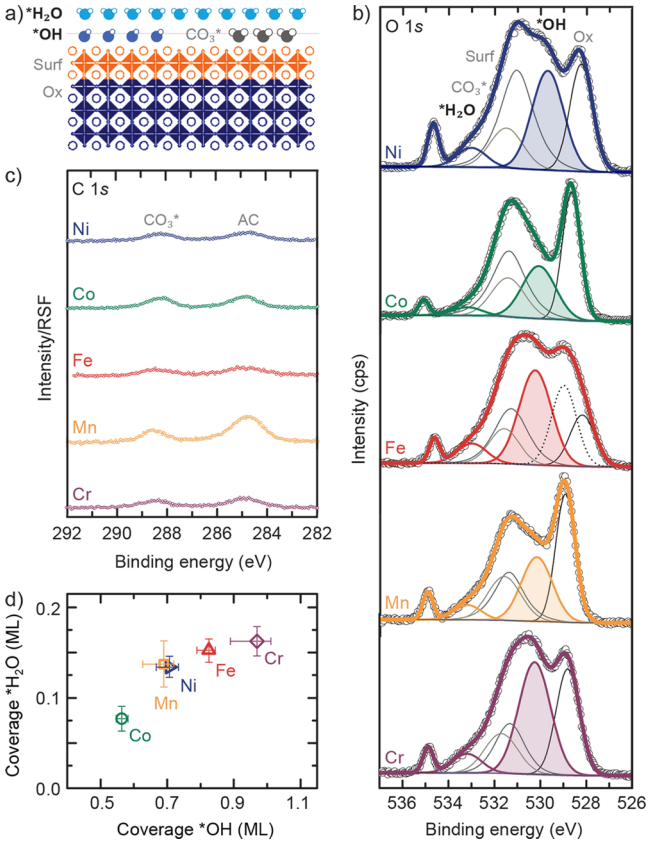

Figure 2. Quantification of adsorbates by AP-XPS. (a) Schematic of the multilayer electron attenuation model used to determine coverages. For further information about the error and deconvolution into bulk "Ox", surface "Surf", carbonates "CO_3*", and gas phase water, see the Supporting Information and ref 23. (b) Fitted O 1s spectra at 25 °C in 0.1 Torr of H_2O. Raw data in counts per second are shown as circles, and the envelope resulting from the fitted components in bold color; curves are offset for clarity. The *OH intensity is shaded; its relative intensity varies notably with transition metal. (c) Corresponding C 1s spectra, with axis scale taken from (b), adjusted to size, and divided by the experimental O 1s:C 1s relative sensitivity factor (RSF). Shown are the CO_3* component and adventitious carbon (AC). (d) The intensity of the *H_2O peak, outlined in corresponding color in (c), scales with that of *OH. Error bars are defined as the 95% confidence intervals estimated from Monte Carlo simulations.

intermediate BE ~1.3 eV higher than the bulk is a feature attributable to *OH species.[9,45,46] A carbonate feature became present at higher RH, also at ~2.8 eV above the bulk oxide.[47] The O 1s carbonate contribution was determined from the C 1s integrated area for carbonate, employing an experimentally measured relative sensitivity factor and assuming a 3:1 O:C carbonate stoichiometry (Figure 2c). The intensity of *OH increased as the sample was cooled to access higher RH, further supporting the peak assignment. At high RH, water adsorbed on the surface, *H_2O, with a BE at ~533.3 eV.[9,45] In addition, the gas phase H_2O peak is observed at a water partial pressure of 0.1 Torr. Thus, by analyzing the evolution of the O 1s and C 1s spectra with RH, the spectra were deconvoluted into different oxygen groups on the surface (Table S4).[23]

The perovskite surfaces react with water to form hydroxyl groups, which is evidenced by notable *OH contribution in the O 1s spectra with increasing RH. The degree of hydroxylation on the perovskite surface is dependent on the transition metal ion: lower intensities of *OH species on $LaMnO_3$ and $LaCoO_3$ than on the other three films are clearly visible in the O 1s spectra, as shown in Figure 2b (Table S6). The coverage of *OH and adsorbed *H_2O under the highest RH of the isobar was extracted using a multilayer model proposed recently[23,48] (Figure 2a, Tables S4 and S5). The *OH coverage increases in the order of Co < Mn < Ni < Fe < Cr, where a difference up to half a monolayer (ML) reflects significantly different affinities of LaMO_3 toward hydroxylation and binding strengths of *OH. The coverage of *OH was also found to scale with adsorbed *H_2O, as shown in Figure 2d, which suggests that water can interact strongly with hydroxyl groups on the surface. Below we discuss how the interactions between water and LaMO_3—specifically the coverage of *OH and *H_2O—may influence macroscopic wetting and ORR activity in basic solution.

Influence of *OH on Macroscopic Wetting. We first show that the receding contact angle of water in macroscopic wetting trends with the surface coverage of *OH groups on LaMO_3 measured by AP-XPS. The macroscopic interaction of LaMO_3 film surfaces with water was measured by the advancing and receding contact angle. Wetting hysteresis can provide insights into the chemical nature of the water/oxide interface as the contact line experiences different interactions during advancing and receding motion.[49]

All surfaces were moderately hydrophobic in contact with water with advancing angles of ~90°, with the exception of $LaCrO_3$ ~70° (Figure 3a). We attribute the difference in

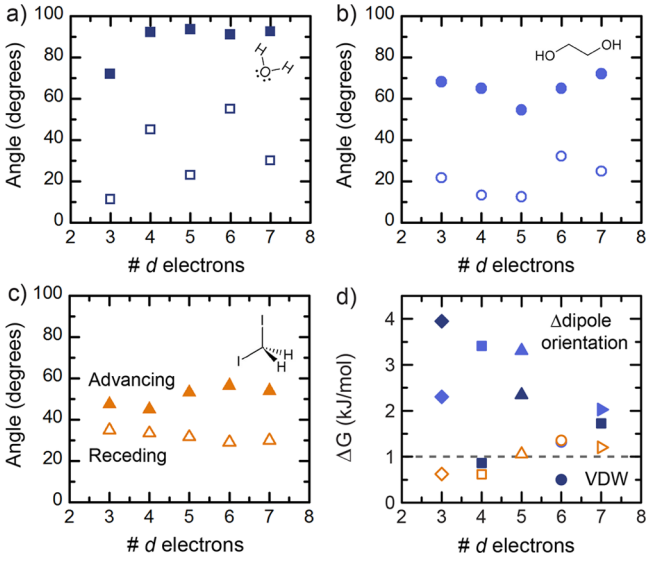

Figure 3. Advancing (solid) and receding (open) contact angles on LaMO_3 surfaces, with M of different d-electron number. The probe liquid was (a) dipolar water, dark blue; (b) monopolar ethylene glycol, medium blue; or (c) apolar diiodomethane, orange. (d) The free energy of hysteresis, ΔG, obtained from the advancing and receding angle of each liquid in corresponding color, is large in magnitude (≥1 kJ/mol) for polar solvents, indicative of reorientation of polar surface groups.

wettability to the presence of Cr^{6+} when exposed to O_2 gas and its readiness to reduce to Cr^{3+} upon wetting (Figures S6 and S7). This is in contrast to other transition metals in the form of LaMO_3, which remain nominally in the 3+ valence state upon exposure to O_2 gas, and are more resistant to oxidation (Figure S7). The higher oxidation state of Cr leads to a more electronegative transition metal center (higher reduction

DOI: 10.1021/acs.jpcc.5b06621
J. Phys. Chem. C 2015, 119, 18504−18512

potential), promoting electron transfer upon interaction with H_2O and expected to wet more readily than other $LaMO_3$ surfaces, where M retains the 3+ valence state on the surface. The oxidized $LaCrO_3$ surface can also be considered more acidic,[50] which promotes wetting.[51]

In contrast to the advancing angles, the receding contact angles of all $LaMO_3$ were notably lower and strongly dependent on the transition metal. Although the difference in the advancing and receding angles is not fully understood at the molecular scale, it is postulated that receding water must break the H-bonds[49] that have formed between surface polar groups and water, thus leading to stronger interaction with water and a lower receding angle[52] than advancing. To assess this hypothesis, we consider the polar contributions of the oxide surface to dewetting.

For interactions between a solid and a liquid, the change in free energy can be considered as the sum of that arising from apolar Lifshitz–van der Waals (γ^{LW}) interactions and from polar acid–base interactions. The polar interactions depend on the electron-accepting (γ^+) and electron-donating (γ^-) contributions from both surface and probe liquid.[53−55] Thus, by measuring the contact angle with three probe liquids of known apolar and polar components and surface tension (Table S7), all components of surface energy can be quantified using the van Oss–Chaudhury–Good approach.[55,56] The resultant contact angles for each liquid are shown in Figure 3. The advancing angle was highest for polar liquids and depended weakly on the transition metal of $LaMO_3$ surfaces. In contrast, the receding contact angle varied notably with M for a polar probe but remained approximately constant for all surfaces probed with apolar DIM. Notable hysteresis was seen in the contact angle of polar H_2O and EG, in contrast to that of DIM.

The associated free energy of hysteresis in wetting enables a direct experimental comparison of the strength of interaction between the surface and probe liquids of different polar character. The free energy of hysteresis for apolar DIM is ∼1 kJ/mol and varies little with d-electron number, while for polar EG and H_2O it spans from ∼1 to 4 kJ/mol (Figure 3d). This range is comparable to that attributed to conformational changes in polar groups[57] and/or strong interactions such as hydrogen bonding.[58] Thus, the large free energy of hysteresis can be attributed to oxygen-containing groups[59] and hydroxyl species.[60] We propose that the large hysteresis observed upon wetting with a polar solvent arises from polar groups at the $LaMO_3$ surface. The $LaMO_3$ (001) surface itself is polar, with alternating planes of LaO (+1 charge) and MO_2 (−1 charge). In contact with the atmosphere, it may compensate for the net surface dipole through numerous mechanisms—including the adsorption of surface species, surface reconstruction, and charge redistribution.[61,62] Upon changing the environment from ambient air (or DIM) to that of a polar medium, the surface compensation will change dramatically due to interaction with this dielectric, giving rise to a large free energy of hysteresis. We hypothesize a change in the polarity of the oxide surface upon wetting can be achieved by orientation of polar *OH groups such that electron-rich oxygen interacts with the positive dipole of the water molecule, yielding low receding contact angle.

The γ^{LW} and γ^+ components were roughly constant for all $LaMO_3$ surfaces for both advancing (Figure 4a) and receding (Figure 4b) contact angles. In contrast, the γ^- component, roughly zero for the advancing angle, was found to be much larger and strongly dependent on the transition metal for the

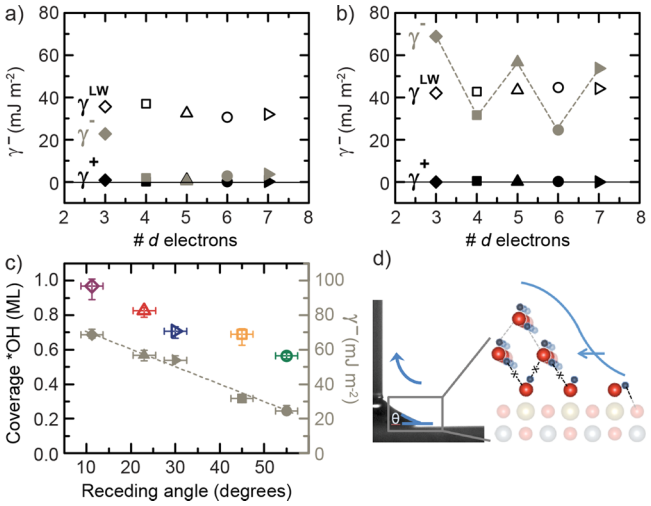

Figure 4. Molecular insight into dewetting and contact angle hysteresis. (a) The apolar (γ^{LW}), electron-accepting (γ^+), and electron-donating component (γ^-) to the advancing contact angle and (b) the receding angle. γ^{LW} and γ^+ do not trend with transition metal or exhibit hysteresis; however, the electron-donating component (γ^-) forms a W shape with d-electron number for the receding angle. (c) The receding contact angle is lowest for the surface with the highest coverage of *OH (measured in the most humid condition ∼0.3% RH by AP-XPS, error as in Figure 2) and reflects H-bonding by electron-donating surface groups, γ^-. Error bars were determined from the spread in calculated γ^- resulting from duplicate measurements on the same film. All dotted lines are to guide the eye. (d) Schematic for the receding contact angle, where surface *OH groups can reorient in the polar liquid medium and interact strongly with water. The need to break H bonds is indicated with an "x".

receding contact angle and linearly increases with *OH coverage (Figure 4c). These observations indicate that strong H-bonding interactions at the oxide/water interface lead to lower receding contact angles (Figure 4d). Although lanthanide-containing perovskites are known to have high affinities for carbonate formation,[63] the correlation of receding angle with *OH coverage and measurement of surface energy using carbon-containing probe liquids suggest the receding contact angle reflects strong interactions with polar hydroxyl groups on the surface. Both hydroxyl and water coverage (Figure S8) and electron-donating polarity (Figure 4b) exhibit a W-shape trend with transition metal d-electron number. Inverse W-like trends have been reported among catalytic studies of perovskites such as O_2 adsorption and hydrocarbon oxidation[64] as well as ORR.[11] Here we propose that the polarity of the water/oxide interface can be influenced by the coverage of polar species on the surface and/or the charge distribution of the surface hydroxyl groups. This hypothesis is supported by the fact that decreasing receding angle correlates with increasing both the electron-donating polar contribution to the oxide surface free energy in dewetting and coverage of *OH on $LaMO_3$ measured from AP-XPS (Figure 4c).

Assessing *OH Affinity Theoretically. To further test this hypothesis, we calculated the free energy of adsorption of *OH and *H (dissociated water) on LaO and MO_2 terminations by DFT+U calculations (additional details of the thermodynamic approaches are provided in the Supporting Information), corresponding to the reduction of surface energy upon hydroxylation. The stability of the different species on the two surface terminations, assuming the system is in

DOI: 10.1021/acs.jpcc.5b06621
J. Phys. Chem. C 2015, 119, 18504−18512

thermodynamic equilibrium, should correspond to their relative abundance. Since the surface stability also depends on the chemical potential of metals in the bulk, such a calculation requires definition of the La and *M* chemical potentials. These metal chemical potentials are not independent variables, and their sum is fixed by the condition that the system is in equilibrium with bulk $LaMO_3$. We have compared the (001) LaO and MO_2 surface energy values[65,66] obtained in both the La-rich (system in equilibrium with La_2O_3) and the *M*-rich conditions (system in equilibrium with the MO_x binary oxide compounds) (Figure S9). These two conditions can be considered as the two metal potential limits where the perovskites are stable with respect to the binary oxide compounds. The relative stability of the various hydroxylated surfaces was assessed by comparing the adsorption energy on the LaO surface to that on the MO_2 surface adjusted for the difference in surface energy between the facets; both are referenced to the ideal (001) MO_2 surface at the 1.20 V vs SHE (Figures S10 and S11).

When comparing the adsorption free energy on the two surface terminations, we observe that the LaO surface has a higher affinity for water and hydroxyls groups. To gain insight into more humid environments, we then compute the free energies of the hydroxylated surface: a full monolayer of *OH and *OH + *H (dissociated water) on the LaO and MO_2 surfaces, respectively (Figure 5a), both relative to the bare MO_2 surfaces. These hydroxylated surfaces are expected to better reflect the interactions between adsorbates present on a wetted surface. Both adsorption energies exhibit an inverse W shape with the number of d electrons, accounting for the differences in surface energy compared to the bare MO_2 surface. This trend in the reduction of surface energy upon hydroxylation is reflected in the ease of removing a macroscopic droplet of water.

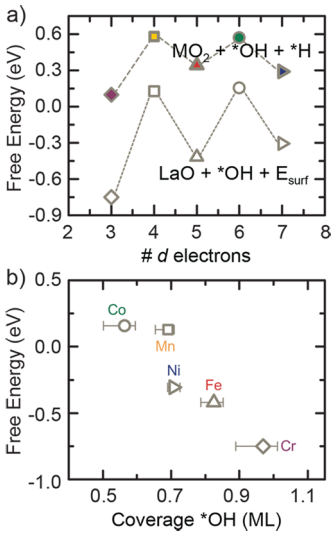

Figure 5. Density functional theory (DFT) calculations of hydroxylation energetics accounting for the difference in surface energies compared to the bare MO_2 surface at the condition of $LaMO_3$ in equilibrium with La_2O_3 (Supporting Information). (a) The DFT-calculated free energies for full coverage of water dissociative adsorption on MO_2 surfaces (filled) and hydroxylation of LaO surfaces (open) show a similar inverse W shape to the receding contact angle. (b) The DFT-calculated free energies for the hydroxylation of LaO surfaces correlates with the coverage measured experimentally by AP-XPS.

The computed surface free energies of the stable hydroxylated LaO termination with 1 monolayer *OH relative to the bare MO_2 surface trends with the experimental coverage measured at 0.3% RH by AP-XPS (Figure 5b). The correlation suggests the coverage from AP-XPS experimentally assesses the relative affinity of a surface toward hydroxylation. The physical origin to different receding angles therefore resides in the transition-metal-dependent affinities toward hydroxyl formation and electron-donating polarity (γ^-) on $LaMO_3$ surfaces.

Implications of *OH on the Oxygen Reduction Reaction. Looking forward to the potential implications of the interaction between *OH and H_2O in designing functional chemistry, we examine these $LaMO_3$ films for aqueous oxygen electrocatalysis, and we report that ORR activity trends inversely with *OH coverage measured under humid conditions. The interaction between *OH and water on the $LaMO_3$ surface can bridge the wetting behavior with their ORR catalytic activity. In basic solution, ORR proceeds on hydroxylated oxide surfaces with a proposed mechanism shown in Figure 6a.[11,67] O_2 displaces *OH (step 1), and subsequent reduction leads to a final step, where water reprotonates the surface (step 4); thus, the binding and coverage of *OH can play an important role in the ORR activity.[14]

We measured the intrinsic activity of the (001)-oriented perovskite films toward the ORR (Figure 6b and Figure S12) using methods established recently,[30] where carbon and binder additives used for oxide powder measurements were not needed. The overpotential, η (kinetic loss), to provide intrinsic ORR current of 40 $\mu A\ cm^{-2}_{ox}$ was found to increase from *M* = Co, Mn to Ni. For the inactive *M* = Fe and Cr, meaningful current densities could not be obtained without potential reduction of the oxide due to the lack of carbon ORR current. Interestingly, the ORR activity trends inversely with the coverage of *OH measured by AP-XPS, where the most active catalyst $LaCoO_3$ has the smallest amount of *OH (Figure 6c). Although the absolute coverage of *OH depends on pH,[1,68] this trend of *OH on $LaMO_3$ measured in water vapor gauges the relative affinity of these surfaces toward hydroxylation. Greater *OH coverage, indicative of an increased binding strength of *OH, can hinder the displacement of *OH by molecular oxygen (step 1 in Figure 6a), which is considered to be rate-limiting for ORR,[11] and lower ORR activity.

CONCLUSIONS

In summary, we establish the molecular descriptor of *OH coverage for both the receding contact angle and ORR activity. Increasing *OH coverage on perovskites correlates with lower receding contact angle, greater electron-donor character of the surface, and lower ORR activity. We show for the first time that the tendency of a polar $LaMO_3$ surface toward hydroxylation can influence macroscopic wetting properties and oxygen electrocatalysis. We note that extension of these trends to broader classes of surfaces and ranges of hydroxyl affinity requires further investigation; however, current understanding suggests that the design of highly active ORR catalysts should consider the intrinsic hydrophobicity of oxide chemistries and their tendency to hydroxylate. Thus, this study opens a new door to study and exploit hydrogen bonding on polar surfaces to design functionality at the solid/water interface.

DOI: 10.1021/acs.jpcc.5b06621
J. Phys. Chem. C 2015, 119, 18504−18512

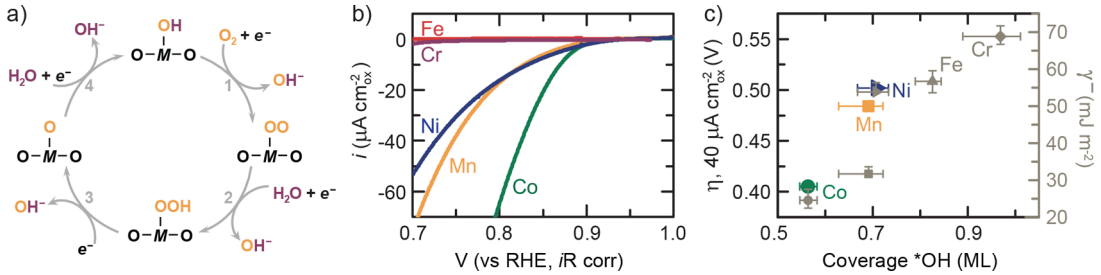

Figure 6. Affinity toward hydroxylation describes ORR and wetting. (a) Schematic of the mechanism for the oxygen reduction reaction (ORR) proposed by Suntivich et al.[11] and Goodenough et al.,[67] noting the *OH species between steps 4 and 1. (b) Capacitance-corrected cyclic voltammetry at 10 mV/s in O_2-saturated 0.1 M KOH. (c) The overpotential (η) required to achieve a given ORR current, extracted from CVs, correlates with the coverage of *OH (left axis), where an inactive surface is more hydroxylated, with a higher electron-donating component (γ^-) to dewetting (right axis, error as in Figure 4). ORR activity of $LaCrO_3$ and $LaFeO_3$ is too low to obtain meaningful current without potential reduction of the oxide due to the lack of carbon ORR current.

■ ASSOCIATED CONTENT

Supporting Information

Further experimental details, additional characterization and measurements, and details of calculations. The Supporting Information is available free of charge on the ACS Publications website at DOI: 10.1021/acs.jpcc.5b06621.

■ AUTHOR INFORMATION

Corresponding Authors

*E-mail varanasi@mit.edu (K.K.V).
*E-mail shaohorn@mit.edu (Y.S.-H.).

Present Address

▽G.A.: Chemical Engineering and Applied Chemistry Department, University of Toronto, Toronto, ON M5S3E5.

Notes

The authors declare no competing financial interest.
○M.D.B.: Passed away Dec 20, 2014.

■ ACKNOWLEDGMENTS

This work was supported in part by the MRSEC Program of the NSF under Award DMR-0819762. The ALS and the MES beamline 11.0.2 are supported by the Director, Office of Science, Office of Basic Energy Sciences, Division of Chemical Sciences, Geosciences, and Biosciences and Materials Sciences Division of the US DOE at the Lawrence Berkeley National Laboratory under Contract DE-AC02-05CH11231. The PLD film growth was conducted at the Center for Nanophase Materials Sciences, a DOE Office of Science User Facility. Computations benefited from use of the National Energy Research Scientific Computing Center allocation at Oak Ridge National Laboratory. K.A.S. was supported in part by the NSF Graduate Research Fellowship under Grant DGE-1122374. K.K.V. acknowledges the support from NSF Career Award (0952564). We thank Srinivas P. B. Subramanyam and Andrey Shavorskiy for experimental assistance and Milind Gadre and Dane Morgan for helpful discussions.

■ REFERENCES

(1) Brown, G. E.; Henrich, V. E.; Casey, W. H.; Clark, D. L.; Eggleston, C.; Felmy, A.; Goodman, D. W.; Grätzel, M.; Maciel, G.; McCarthy, M. I.; Nealson, K. H.; Sverjensky, D. A.; Toney, M. F.; Zachara, J. M. Metal Oxide Surfaces and Their Interactions with Aqueous Solutions and Microbial Organisms. *Chem. Rev.* **1999**, *99*, 77−174.

(2) Kuhlenbeck, H.; Shaikhutdinov, S.; Freund, H.-J. Well-Ordered Transition Metal Oxide Layers in Model Catalysis − A Series of Case Studies. *Chem. Rev.* **2013**, *113*, 3986−4034.

(3) Gray, H. B. Powering the planet with solar fuel. *Nat. Chem.* **2009**, *1*, 7−7.

(4) Chorkendorff, I.; Niemantsverdriet, J. W. *Concepts of Modern Catalysis and Kinetics*; Wiley-VCH: Weinheim, Germany, 2003.

(5) Azimi, G.; Dhiman, R.; Kwon, H.-M.; Paxson, A. T.; Varanasi, K. K. Hydrophobicity of Rare-Earth Oxide Ceramics. *Nat. Mater.* **2013**, *12*, 315−320.

(6) Thiel, P. A.; Madey, T. E. The Interaction of Water with Solid Surfaces: Fundamental Aspects. *Surf. Sci. Rep.* **1987**, *7*, 211−385.

(7) Henderson, M. A. The Interaction of Water with Solid Surfaces: Fundamental Aspects Revisited. *Surf. Sci. Rep.* **2002**, *46*, 1−308.

(8) Giovambattista, N.; Debenedetti, P. G.; Rossky, P. J. Effect of Surface Polarity on Water Contact Angle and Interfacial Hydration Structure. *J. Phys. Chem. B* **2007**, *111*, 9581−9587.

(9) Ketteler, G.; Yamamoto, S.; Bluhm, H.; Andersson, K.; Starr, D. E.; Ogletree, D. F.; Ogasawara, H.; Nilsson, A.; Salmeron, M. The Nature of Water Nucleation Sites on TiO_2(110) Surfaces Revealed by Ambient Pressure X-ray Photoelectron Spectroscopy. *J. Phys. Chem. C* **2007**, *111*, 8278−8282.

(10) Rossmeisl, J.; Qu, Z. W.; Zhu, H.; Kroes, G. J.; Nørskov, J. K. Electrolysis of Water on Oxide Surfaces. *J. Electroanal. Chem.* **2007**, *607*, 83−89.

(11) Suntivich, J.; Gasteiger, H. A.; Yabuuchi, N.; Nakanishi, H.; Goodenough, J. B.; Shao-Horn, Y. Design Principles for Oxygen-Reduction Activity on Perovskite Oxide Catalysts for Fuel Cells and Metal−Air Batteries. *Nat. Chem.* **2011**, *3*, 546−550.

(12) Suntivich, J.; May, K. J.; Gasteiger, H. A.; Goodenough, J. B.; Shao-Horn, Y. A Perovskite Oxide Optimized for Oxygen Evolution Catalysis from Molecular Orbital Principles. *Science* **2011**, *334*, 1383−1385.

(13) Subbaraman, R.; Tripkovic, D.; Chang, K.-C.; Strmcnik, D.; Paulikas, A. P.; Hirunsit, P.; Chan, M.; Greeley, J.; Stamenkovic, V.; Markovic, N. M. Trends in Activity for the Water Electrolyser Reactions on 3*d* M(Ni,Co,Fe,Mn) Hydr(oxy)oxide Catalysts. *Nat. Mater.* **2012**, *11*, 550−557.

(14) Man, I. C.; Su, H.-Y.; Calle-Vallejo, F.; Hansen, H. A.; Martínez, J. I.; Inoglu, N. G.; Kitchin, J.; Jaramillo, T. F.; Nørskov, J. K.; Rossmeisl, J. Universality in Oxygen Evolution Electrocatalysis on Oxide Surfaces. *ChemCatChem* **2011**, *3*, 1159−1165.

(15) Granick, S.; Bae, S. C. A Curious Antipathy for Water. *Science* **2008**, *322*, 1477−1478.

(16) Diebold, U.; Li, S.-C.; Schmid, M. Oxide Surface Science. *Annu. Rev. Phys. Chem.* **2010**, *61*, 129−148.

(17) Flavell, W. R.; Thomas, A. G.; Hollingworth, J.; Warren, S.; Grice, S. C.; Dunwoody, P. M.; Mitchell, C. E. J.; Marr, P. G. D.; Teehan, D.; Downes, S.; Seddon, E. A.; Dhanak, V. R.; Asai, K.; Koboyashi, Y.; Yamada, N. Electronic Structure and Surface Reactivity of $La_{1-x}Sr_xCoO_3$. *Faraday Discuss.* **1999**, *114*, 407−420.

DOI: 10.1021/acs.jpcc.5b06621
J. Phys. Chem. C 2015, 119, 18504−18512

(18) Wang, Z.; Hao, X.; Gerhold, S.; Novotny, Z.; Franchini, C.; McDermott, E.; Schulte, K.; Schmid, M.; Diebold, U. Water Adsorption at the Tetrahedral Titania Surface Layer of $SrTiO_3(110)$-(4 × 1). *J. Phys. Chem. C* **2013**, *117*, 26060−26069.
(19) Ogletree, D. F.; Bluhm, H.; Lebedev, G.; Fadley, C. S.; Hussain, Z.; Salmeron, M. A Differentially Pumped Electrostatic Lens System for Photoemission Studies in the Millibar Range. *Rev. Sci. Instrum.* **2002**, *73*, 3872−3877.
(20) Starr, D. E.; Liu, Z.; Havecker, M.; Knop-Gericke, A.; Bluhm, H. Investigation of Solid/Vapor Interfaces Using Ambient Pressure X-ray Photoelectron Spectroscopy. *Chem. Soc. Rev.* **2013**, *42*, 5833−5857.
(21) Salmeron, M.; Schlögl, R. Ambient Pressure Photoelectron Spectroscopy: A New Tool for Surface Science and Nanotechnology. *Surf. Sci. Rep.* **2008**, *63*, 169−199.
(22) Proyer, S.; Stangl, E.; Borz, M.; Hellebrand, B.; Bäuerle, D. Particulates on Pulsed-Laser Deposited Y-Ba-Cu-O Films. *Phys. C* **1996**, *257*, 1−15.
(23) Stoerzinger, K. A.; Hong, W. T.; Crumlin, E. J.; Bluhm, H.; Biegalski, M. D.; Shao-Horn, Y. Water Reactivity on the $LaCoO_3$ (001) Surface: An Ambient Pressure X-ray Photoelectron Spectroscopy Study. *J. Phys. Chem. C* **2014**, *118*, 19733−19741.
(24) Ogletree, D. F.; Bluhm, H.; Hebenstreit, E. D.; Salmeron, M. Photoelectron Spectroscopy under Ambient Pressure and Temperature Conditions. *Nucl. Instrum. Methods Phys. Res., Sect. A* **2009**, *601*, 151−160.
(25) Whaley, J. A.; McDaniel, A. H.; El Gabaly, F.; Farrow, R. L.; Grass, M. E.; Hussain, Z.; Liu, Z.; Linne, M. A.; Bluhm, H.; McCarty, K. F. Note: Fixture for Characterizing Electrochemical Devices in-Operando in Traditional Vacuum Systems. *Rev. Sci. Instrum.* **2010**, *81*, 086104−3.
(26) Andersson, K.; Nikitin, A.; Pettersson, L. G. M.; Nilsson, A.; Ogasawara, H. Water Dissociation on Ru(001): An Activated Process. *Phys. Rev. Lett.* **2004**, *93*, 196101.
(27) Yates, J. T., Jr. Photochemistry on TiO_2: Mechanisms Behind the Surface Chemistry. *Surf. Sci.* **2009**, *603*, 1605−1612.
(28) McCafferty, E.; Wightman, J. P. Determination of the Concentration of Surface Hydroxyl Groups on Metal Oxide Films by a Quantitative XPS Method. *Surf. Interface Anal.* **1998**, *26*, 549−564.
(29) Kurbatov, G.; Darque-Ceretti, E.; Aucouturier, M. Characterization of Hydroxylated Oxide Film on Iron Surfaces and its Acid−Base Properties using XPS. *Surf. Interface Anal.* **1992**, *18*, 811−820.
(30) Stoerzinger, K. A.; Risch, M.; Suntivich, J.; Lu, W. M.; Zhou, J.; Biegalski, M. D.; Christen, H. M.; Ariando; Venkatesan, T.; Shao-Horn, Y. Oxygen Electrocatalysis on (001)-Oriented Manganese Perovskite Films: Mn Valency and Charge Transfer at the Nanoscale. *Energy Environ. Sci.* **2013**, *6*, 1582−1588.
(31) Anisimov, V. I.; Aryasetiawan, F.; Lichtenstein, A. I. First-Principles Calculations of the Electronic Structure and Spectra of Strongly Correlated Systems: The LDA + U Method. *J. Phys.: Condens. Matter* **1997**, *9*, 767.
(32) Dudarev, S. L.; Botton, G. A.; Savrasov, S. Y.; Humphreys, C. J.; Sutton, A. P. Electron-Energy-Loss Spectra and the Structural Stability of Nickel Oxide:An LSDA+U Study. *Phys. Rev. B: Condens. Matter Mater. Phys.* **1998**, *57*, 1505−1509.
(33) Kresse, G.; Furthmüller, J. Efficient Iterative Schemes for *Ab Initio* Total-Energy Calculations Using a Plane-Wave Basis Set. *Phys. Rev. B: Condens. Matter Mater. Phys.* **1996**, *54*, 11169−11186.
(34) Kresse, G.; Hafner, J. Ab Initio Molecular Dynamics for Liquid Metals. *Phys. Rev. B: Condens. Matter Mater. Phys.* **1993**, *47*, 558−561.
(35) Blöchl, P. E. Projector Augmented-Wave Method. *Phys. Rev. B: Condens. Matter Mater. Phys.* **1994**, *50*, 17953−17979.
(36) Perdew, J. P.; Chevary, J. A.; Vosko, S. H.; Jackson, K. A.; Pederson, M. R.; Singh, D. J.; Fiolhais, C. Atoms, Molecules, Solids, and Surfaces: Applications of the Generalized Gradient Approximation for Exchange and Correlation. *Phys. Rev. B: Condens. Matter Mater. Phys.* **1992**, *46*, 6671−6687.
(37) Wang, L.; Maxisch, T.; Ceder, G. Oxidation Energies of Transition Metal Oxides within the GGA+U Framework. *Phys. Rev. B: Condens. Matter Mater. Phys.* **2006**, *73*, 195107.
(38) Lee, Y.-L.; Kleis, J.; Rossmeisl, J.; Morgan, D. Ab Initio Energetics of $LaBO_3$ (001) (*B* = Mn, Fe, Co, and Ni) for Solid Oxide Fuel Cell Cathodes. *Phys. Rev. B: Condens. Matter Mater. Phys.* **2009**, *80*, 224101.
(39) Koehler, W. C.; Wollan, E. O. Neutron-Diffraction Study of the Magnetic Properties of Perovskite-Like Compounds $LaBO_3$. *J. Phys. Chem. Solids* **1957**, *2*, 100−106.
(40) Elemans, J. B. A. A.; Van Laar, B.; Van Der Veen, K. R.; Loopstra, B. O. The Crystallographic and Magnetic Structures of $La_{1-x}Ba_xMn_{1-x}Me_xO_3$ (Me = Mn or Ti). *J. Solid State Chem.* **1971**, *3*, 238−242.
(41) Geller, S.; Wood, E. A. Crystallographic Studies of Perovskite-Like Compounds. I. Rare Earth Orthoferrites and $YFeO_3$, $YCrO_3$, $YAlO_3$. *Acta Crystallogr.* **1956**, *9*, 563−568.
(42) Thornton, G.; Tofield, B. C.; Hewat, A. W. A Neutron Diffraction Study of $LaCoO_3$ in the Temperature Range 4.2 < *T* < 1248 K. *J. Solid State Chem.* **1986**, *61*, 301−307.
(43) Goodenough, J. B. Localized versus Collective *d* Electrons and Néel Temperatures in Perovskite and Perovskite-Related Structures. *Phys. Rev.* **1967**, *164*, 785−789.
(44) Lee, Y.-L.; Kleis, J.; Rossmeisl, J.; Shao-Horn, Y.; Morgan, D. Prediction of Solid Oxide Fuel Cell Cathode Activity with First-Principles Descriptors. *Energy Environ. Sci.* **2011**, *4*, 3966−3970.
(45) Yamamoto, S.; Kendelewicz, T.; Newberg, J. T.; Ketteler, G.; Starr, D. E.; Mysak, E. R.; Andersson, K. J.; Ogasawara, H.; Bluhm, H.; Salmeron, M.; Brown, G. E.; Nilsson, A. Water Adsorption on α-$Fe_2O_3(0001)$ at near Ambient Conditions. *J. Phys. Chem. C* **2010**, *114*, 2256−2266.
(46) Kendelewicz, T.; Kaya, S.; Newberg, J. T.; Bluhm, H.; Mulakaluri, N.; Moritz, W.; Scheffler, M.; Nilsson, A.; Pentcheva, R.; Brown, G. E. X-ray Photoemission and Density Functional Theory Study of the Interaction of Water Vapor with the $Fe_3O_4(001)$ Surface at Near-Ambient Conditions. *J. Phys. Chem. C* **2013**, *117*, 2719−2733.
(47) Stoch, J.; Gablankowska-Kukucz, J. The Effect of Carbonate Contaminations on the XPS O 1s Band Structure in Metal Oxides. *Surf. Interface Anal.* **1991**, *17*, 165−167.
(48) Newberg, J. T.; Starr, D. E.; Yamamoto, S.; Kaya, S.; Kendelewicz, T.; Mysak, E. R.; Porsgaard, S.; Salmeron, M. B.; Brown, G. E., Jr.; Nilsson, A.; Bluhm, H. Formation of Hydroxyl and Water Layers on MgO Films Studied with Ambient Pressure XPS. *Surf. Sci.* **2011**, *605*, 89−94.
(49) Extrand, C. W. Contact Angles and Their Hysteresis as a Measure of Liquid−Solid Adhesion. *Langmuir* **2004**, *20*, 4017−4021.
(50) Connell, G.; Dumesic, J. A. Acidic Properties of Binary Oxide Catalysts: I. Mössbauer Spectroscopy and Pyridine Adsorption for Iron Supported on Silica. *J. Catal.* **1986**, *101*, 103−113.
(51) Lee, T. R.; Carey, R. I.; Biebuyck, H. A.; Whitesides, G. M. The Wetting of Monolayer Films Exposing Ionizable Acids and Bases. *Langmuir* **1994**, *10*, 741−749.
(52) de Gennes, P.-G.; Brochard-Wyart, F.; Quéré, D. Dewetting. In *Capillarity and Wetting Phenomena*; Springer: New York, 2004; pp 153−190.
(53) van Oss, C. J.; Chaudhury, M. K.; Good, R. J. Monopolar Surfaces. *Adv. Colloid Interface Sci.* **1987**, *28*, 35−64.
(54) Van Oss, C. J.; Good, R. J.; Chaudhury, M. K. The Role of van der Waals Forces and Hydrogen Bonds in "Hydrophobic Interactions" between Biopolymers and Low Energy Surfaces. *J. Colloid Interface Sci.* **1986**, *111*, 378−390.
(55) Van Oss, C. J.; Ju, L.; Chaudhury, M. K.; Good, R. J. Estimation of the Polar Parameters of the Surface Tension of Liquids by Contact Angle Measurements on Gels. *J. Colloid Interface Sci.* **1989**, *128*, 313−319.
(56) Good, R. J. Contact Angle, Wetting, and Adhesion: A Critical Review. *J. Adhes. Sci. Technol.* **1992**, *6*, 1269−1302.
(57) Volkenstein, M. V. *Configurational Statistics of Polymeric Chains*; Wiley: New York, 1963.

DOI: 10.1021/acs.jpcc.5b06621
J. Phys. Chem. C 2015, 119, 18504−18512

(58) Fowkes, F. *Surface and Interfacial Aspects of Biomedical Polymers*; Springer: New York, 1985.
(59) Morra, M.; Occhiello, E.; Garbassi, F. Contact Angle Hysteresis on Oxygen Plasma Treated Polypropylene Surfaces. *J. Colloid Interface Sci.* **1989**, *132*, 504−508.
(60) Bain, C. D.; Evall, J.; Whitesides, G. M. Formation of Monolayers by the Coadsorption of Thiols on Gold: Variation in the Head Group, Tail Group, and Solvent. *J. Am. Chem. Soc.* **1989**, *111*, 7155−7164.
(61) Noguera, C. Polar Oxide Surfaces. *J. Phys.: Condens. Matter* **2000**, *12*, R367.
(62) Tasker, P. W. The Stability of Ionic Crystal Surfaces. *J. Phys. C: Solid State Phys.* **1979**, *12*, 4977.
(63) Tascon, J. M. D.; Tejuca, L. G. Adsorption of CO_2 on the Perovskite-Type Oxide $LaCoO_3$. *J. Chem. Soc., Faraday Trans. 1* **1981**, *77*, 591−602.
(64) Kremenic, G.; Nieto, J. M. L.; Tascon, J. M. D.; Tejuca, L. G. Chemisorption and Catalysis on $LaMO_3$ Oxides. *J. Chem. Soc., Faraday Trans. 1* **1985**, *81*, 939−949.
(65) Reuter, K.; Scheffler, M. Composition, Structure, and Stability of RuO_2 (110) as a Function of Oxygen Pressure. *Phys. Rev. B: Condens. Matter Mater. Phys.* **2001**, *65*, 035406.
(66) Johnston, K.; Castell, M. R.; Paxton, A. T.; Finnis, M. W. $SrTiO_3$ (001) (2 × 1) Reconstructions:First-Principles Calculations of Surface Energy and Atomic Structure Compared with Scanning Tunneling Microscopy Images. *Phys. Rev. B: Condens. Matter Mater. Phys.* **2004**, *70*, 085415.
(67) Goodenough, J. B.; Manoharan, R.; Paranthaman, M. Surface Protonation and Electrochemical Activity of Oxides in Aqueous Solution. *J. Am. Chem. Soc.* **1990**, *112*, 2076−2082.
(68) Boehm, H. P. Acidic and Basic Properties of Hydroxylated Metal Oxide Surfaces. *Discuss. Faraday Soc.* **1971**, *52*, 264−275.

DOI: 10.1021/acs.jpcc.5b06621
J. Phys. Chem. C 2015, 119, 18504−18512